GPS Constraints on Drought-Induced Groundwater Loss Around Great Salt Lake, Utah, with Implications for Seismicity Modulation

Zachary Young[1,1], Corné Kreemer[2,2], and Geoffrey Blewitt[1,1]

[1]University of Nevada, Reno
[2]University of Nevada Reno

January 20, 2023

Abstract

Great Salt Lake (GSL), Utah, lost 1.89 +/- 0.04 meters of water during the 2012 to 2016 drought. During this timeframe, data from the GRACE mission do not detect anomalous mass loss, but nearby Global Positioning System (GPS) stations show significant shifts in position. We find that crustal deformation, from unloading the Earth's crust with the observed GSL water loss alone, does not explain the GPS displacements, suggesting contributions from additional water storage loss surrounding GSL. This study applies a damped least squares inversion to the 3D GPS displacements to test a range of distributions of radial mass load rings to fit the observations. When considering the horizontal and vertical displacements simultaneously, we find the most realistic distribution of water loss while also resolving the observed water loss of the lake. Our preferred model identifies radially decreasing mass loss up to 64 km from the lake. The contribution of exterior groundwater loss is substantial (10.9 +/- 2.8 km^3 vs. 5.5 +/- 1.0 km^3 on the lake), and greatly improves the fit to the observations. Nearby groundwater wells exhibit significant water loss during the drought, which substantiates the presence of significant water loss outside of the lake, but also highlights greater spatial variation than our model can resolve. We observe seismicity modulation within the inferred load region, while the region outside the (un)loading reveals no significant modulation. Drier periods exhibit higher quantities of events than wetter periods and changes in trend of the earthquake rate are correlated with regional mass trends.

GPS Constraints on Drought-Induced Groundwater Loss Around Great Salt Lake, Utah, with Implications for Seismicity Modulation

Zachary Young[1], Corné Kreemer[1], Geoffrey Blewitt[1]

[1]Nevada Geodetic Laboratory, Nevada Bureau of Mines and Geology, University of Nevada, Reno, Reno, Nevada, USA

Corresponding author: Zachary Young (zyoung@nevada.unr.edu)

Key Points:

- 3D time-series of local GPS stations are sensitive to mass loss in Great Salt Lake and additional groundwater contributions nearby.
- During the 2012 – 2016 drought, the Great Salt Lake basin lost 10.9 ± 2.8 km^3 of groundwater while the lake itself lost 5.5 ± 1.0 km^3.
- Seismicity near Great Salt Lake is modulated throughout the drought cycle with significantly more events occurring during drought periods.

This manuscript has been submitted for consideration to *Journal of Geophysical Research – Solid Earth*, on March 6, 2021.

Abstract

Great Salt Lake (GSL), Utah, lost 1.89 ± 0.04 meters of water during the 2012 to 2016 drought. During this timeframe, data from the GRACE mission do not detect anomalous mass loss, but nearby Global Positioning System (GPS) stations show significant shifts in position. We find that crustal deformation, from unloading the Earth's crust with the observed GSL water loss alone, does not explain the GPS displacements, suggesting contributions from additional water storage loss surrounding GSL. This study applies a damped least squares inversion to the 3D GPS displacements to test a range of distributions of radial mass load rings to fit the observations. When considering the horizontal and vertical displacements simultaneously, we find the most realistic distribution of water loss while also resolving the observed water loss of the lake. Our preferred model identifies radially decreasing mass loss up to 64 km from the lake. The contribution of exterior groundwater loss is substantial (10.9 ± 2.8 km^3 vs. 5.5 ± 1.0 km^3 on the lake), and greatly improves the fit to the observations. Nearby groundwater wells exhibit significant water loss during the drought, which substantiates the presence of significant water loss outside of the lake, but also highlights greater spatial variation than our model can resolve. We observe seismicity modulation within the inferred load region, while the region outside the (un)loading reveals no significant modulation. Drier periods exhibit higher quantities of events than wetter periods and changes in trend of the earthquake rate are correlated with regional mass trends.

Plain Language Summary

During the 2012 – 2016 drought, GPS stations near Great Salt Lake (GSL), UT, showed a distinct shift in position. The GSL lost nearly two meters of water. As water mass is lost from a lake, the crust uplifts and extends from the center of the source; however, the amount of water loss observed on the GSL is not enough to explain the displacements observed by nearby GPS stations. To address this, water loss in the form of additional rings of groundwater surrounding the GSL are estimated and we find the model that best fits the GPS displacements. We find that water loss up to 64 km from the edge of the lake contributes to the observed signal, at a volume substantially larger than lost on the lake itself. Our results show that GPS data can be used to infer localized water loss and discriminate between loss of surface water versus ground water. Furthermore, we see evidence that changes in mass in the region result in changes in the quantity and rate of seismicity; significantly more events occur in the crust underneath the area with water fluctuations when there is a reduced water load.

1 Introduction

Decline in fresh water availability is one of many societal challenges resulting from the compounding effects of climate change and population growth (J. S. Famiglietti, 2014; Gleeson et al., 2012; Vörösmarty et al., 2000). Most groundwater loss can be attributed to the increase of pumping for irrigation and other anthropogenic use, particularly during times of drought (Castle et al., 2014; J. S. Famiglietti et al., 2011; Ojha et al., 2019; Matthew Rodell et al., 2009; Russo & Lall, 2017; Scanlon et al., 2012; Tiwari et al., 2009), with depletion rates often highest in land-locked basins within (semi-)arid regions (Wang, 2018). Commensurate with the groundwater loss, significant global surface water loss has also been recorded (Pekel et al., 2016), which is likewise most dramatic for (saline) lakes in (semi-)arid areas (Wurtsbaugh et al., 2017). Regional water loss due to the recent drought in the Western United States has provided insight into the balance between surface (i.e., lakes and reservoirs) and groundwater loss. The ratio of ground to surface water loss has been reported to be 1.89 for the Upper Colorado River basin (Castle et al., 2014), and 4.79 for California's San Joaquin Valley (Ojha et al., 2019).

The Gravity Recovery and Climate Experiment (GRACE) satellite mission has brought invaluable insight into changes in terrestrial water storage (TWS) (e.g., James S. Famiglietti & Rodell, 2013; Rodell et al., 2018). GRACE's wide spatial resolution of ~300 km (Wahr et al., 2013), limits the observations of TWS changes to large regional scales. Even significant deviations localized on relatively small basins, such as Great Salt Lake (GSL), Utah, are virtually undetectable (Rodell & Famiglietti, 1999). Many studies have found Global Positioning System (GPS) data sensitive to mass variation associated with extreme drought conditions (Amos et al., 2014; Argus et al., 2017; Borsa et al., 2014). Changes in load result in an elastic response of the crust which is reflected in both the vertical and horizontal components. While many studies rely primarily on vertical GPS observations to identify and quantify TWS variation, some studies have shown that horizontal motion is a useful indicator of mass localization when regional trends are well accounted for (Fu et al., 2013; Kreemer & Zaliapin, 2018; Wahr et al., 2013).

This study investigates a three-dimensional (3D) transient deformation signal observed at GPS sites near GSL between 2012 and 2016. Onset of this signal correlates well with the beginning of severe drought conditions in the region. During this period, GSL surface elevation decreased by 1.89 ± 0.04 m. Concurrently, GRACE only observes 1.18 ± 0.08 m of equivalent water loss, if the full 300 km resolution is consolidated on the lake, corroborating the findings of Rodell & Famiglietti (1999). While GRACE is unable to quantify the load on the lake for this timeframe, a previous study showed that GPS sites near GSL exhibited load-induced deformation correlated with lake level variation between 1997 and 2003 (Elósegui et al., 2003). Only two long-running GPS sites were available at the time of that study, but results identified the signal in all three components and suggested the need for more complex load geometries. Currently, long-running GPS sites are well distributed around the lake and provide an opportunity to further investigate the sensitivity of 3D GPS near GSL to small spatial scale mass variation (Figure 1). During the recent drought, GPS timeseries reflect horizontal extension and vertical uplift at pairs of stations located in opposite sides of GSL, indicating the presence of an unloading signal (Figure 2). We find that the observed unloading of the lake (consistent with observed lake level drop) underestimates the observed GPS displacements, and that a load on GSL of -5.01 ± 0.26 meters is required to explain the signal (Figures S1 and S2). This is substantially larger than the -1.89 ± 0.04 meters observed on the surface of the lake and unrealistic. Considering the observed ratios of groundwater to surface water shown in previous studies, as well as observed well water level changes during this drought, it is likely that additional groundwater unloading has contributed to the GPS transients. To address this, we estimate displacements due to GSL unloading combined with distributions of groundwater loss and identify the spatial distribution of mass loss in this region that best explains the 3D GPS signal.

2 Observations

Great Salt Lake sits in close proximity to the Wasatch fault to the east (Figure 1). For this study, we only include data within the GSL basin and west of the Wasatch fault. GPS displacements and seismicity on opposing sides of the fault are expected to behave independently and reflect unique dynamics respectively.

2.1 Water Level Variation

Historically, GSL has experienced large fluctuations in lake surface elevation, and the lake level has been in decline since the 1850's (Elósegui et al., 2003; Wurtsbaugh et al., 2017). To investigate the modern trends, we inspect two long running lake elevation gauges (USGS Water Resources, 2020). Deviations in lake elevation compare well with the Palmer Drought Severity Index (PDSI), which provides an index for the intensity of dryness in a region (Abatzoglou et al., 2017) (Figure 2a). In Figure 2, PDSI for the study area is reflected as the background shading and highlights the temporal correlation of dry and wet periods with lake level deviations. The period of 2004 – 2012 (henceforth referred to as our base period), reveals variable drought conditions and minor net change in lake elevation. Between 2012 and 2016 (i.e., the drought period), the PDSI indicates consistent drought conditions and GSL exhibits steady lake level decline, totaling 1.89 ± 0.04 m of surface elevation lost.

The increase in lake level observed at the end of 2016 reveals the combined effects of increased precipitation and anthropogenic modifications. GSL is split by a railroad causeway which separates the lake into northern and southern portions and was retrofitted to improve flow in December of 2016 (Hassibe & Keck, 1991). This has historically caused a difference in water level across the causeway. For the period of 2004 – 2015, the lake elevation in the northern portion showed a consistent ~20-cm lower level than that of the southern half. Between 2015 and 2016, the halves of the lake diverge slightly with the southern portion retaining more water than the northern half. This deviation is not readily distinguishable in the GPS data and is unlikely to influence loading results due to the magnitude and localization of the deviation. For the purpose of this study, we refer to the average of the two stations.

Groundwater well observations reveal a similar pattern of water level decline, with the majority of wells reflecting a distinct trend of water loss during the drought. Well data are obtained from the National Groundwater Monitoring Network, with sites distributed around the majority of GSL (Figure 1) (NGWMN, 2020). Since many wells have poor temporal resolution or inconsistent sampling, three interpretations of the groundwater variation during the drought are provided (Table S1). First, we calculate the Theil-Sen slope and apply it to the duration of the drought (Sen, 1968; Theil, 1950). All wells exhibit water loss during this period and cover a range of water variation between -0.28 and -9.34 meters, and for 22 out 39 available wells, the decline is significant at the 2-standard deviation level, where the standard deviation is calculated as 1.4826 times the median absolute deviation (Huber, 1981). Similar results are observed when applying the MIDAS algorithm to determine the trends while accounting for seasonality (Blewitt et al., 2016). The MIDAS method provides robust estimates, however, only nine stations had enough data points required for this method. Many wells provide data near the start and end times of the drought and investigation of the net difference reveals similar observed ranges to MIDAS. These observations highlight substantial mass variation exterior to the bounds of GSL and exhibit the largest water level deviations at wells closest to the lake.

2.2 GRACE and NLDAS

GRACE data are able to identify spatio-temporal variation of TWS (e.g., Castle et al., 2014; Ojha et al., 2019; Tiwari et al., 2009). Although our study area is below the spatial resolution of GRACE, we inspect the temporal variability of the GRACE signal. Here we use the Release 06 version of GRACE data and select the mascons which span 300 km, centered on GSL (Landerer & Swenson, 2012). Following Sakumura et al. (2014), an ensemble mean solution for the JPL, GFZ, and CSR solutions is calculated for each GRACE mascon. Minimal variation is observed at unique grid points, so we present the average of the timeseries in this study. Figure 2b shows the GRACE data detrended relative to the base period. The data show a 4-year net loss of water mass of 41.1 mm, which is equivalent to only 3.48 ± 0.21 km^3 of water loss. This volume is comparable to only -1.18 ± 0.08 m if the load was entirely constrained to the bounds of the lake. Although the timing of the deviation matches well with the onset of the drought, the volume is significantly smaller than the 5.58 ± 0.11 km^3 implied from the observed lake level decline itself. This indicates that for the small spatial scale of this study, GRACE identifies the regional onset of water loss but does not accurately estimate the magnitude of the loss, supporting the findings of Rodell & Famiglietti (1999).

The North American Land Data Assimilation System Phase 2 (NLDAS-2), provides unique land surface parameters which distinguish surface process variation over time (Xia et al., 2012). Here we use the NLDAS-2 monthly Noah model to observe variation in soil moisture content within the top two meters of soil near GSL (Mocko, 2012). These timeseries show no clear distinction between the base and drought periods (Figure 2c), and indicate that the source of the deviation observed in both the GRACE data and GPS displacements, is not confined to the uppermost soil layers.

2.3 GPS Displacement Fields

The ability of GPS to resolve load variations is highly dependent on the removal of extraneous signals, particularly within the horizontal components (Wahr et al., 2013). To better distinguish the signal attributed to the drought period, contributions of local and regional signals must be taken into account. We address this issue by first identifying well-behaved, long-running, GPS sites in the region. We analyzed GPS station coordinate time-series data that are publicly available at the Nevada Geodetic Laboratory in the IGS14 reference frame (Blewitt et al., 2018). Stations are limited to those which recorded data for the entirety of the drought period as well as four years of data spanning the base period. Three stations, SLCU, ZLC1, and P057, meet the time requirements but exhibit unmodeled transients associated with local aquifer deformation (Hu & Bürgmann, 2020), and/or questionable monumentation. Consequentially, we consider 17 stations in our study area (Figure 1), including stations CEDA and COON, which were investigated by Elósegui et al. (2003). The considered stations provide good spatial coverage around the lake, except to the west of GSL where there are currently no stations installed.

Regional common mode variation in the GPS positions can alter the inferred displacement field and is a source of error for our study (Kreemer & Blewitt, 2021; Li et al., 2020; Márquez-Azúa & DeMets, 2003; Serpelloni et al., 2013). We are interested uniquely in how the GSL area affects the GPS positions and not how the positions may be affected by more large-scale signals. We therefore use nineteen long-running regional stations outside our study area with limited data gaps (see inset of Figure 1), to calculate the regional common mode component (CMC). Station timeseries are detrended, and the CMC is defined as the median position at each epoch and removed from our study timeseries. A comparison of GPS observations is shown in Figure 2d. These timeseries are detrended relative to the base period, with the common mode, annual, and semi-annual components removed. A consistent change in trend is present for the duration of the drought period in all three components. Each pair of stations are positioned on opposite sides of the lake, as identified in Figure 1, revealing east-west and north-south extension with vertical uplift.

To distinguish the unique displacements attributed to the drought period, long term trends, due to both tectonic and non-tectonic sources, must be removed from each timeseries. Individual velocities of the cleaned timeseries, for both the base and drought periods, are calculated using MIDAS. This algorithm is robust to outliers, steps, and annual signals in the timeseries. The drought relative to base-period velocities are then multiplied by the duration of the drought period. Signals which are consistent across both periods (such as the long-term tectonic loading) are removed by this approach, identifying the net displacements attributed to the drought period.

The resulting GPS drought-specific displacement field shows motion consistent with an unloading signal centered on/near GSL (Figure 3). Horizontal displacements exhibit extension across the lake. All stations exhibit vertical uplift, with the largest displacements at stations located closest to the lake. We note that stations to the south of the GSL exhibit more scatter than their counterparts to the north.

3 Groundwater Loading Model

3.1 Elastic Loading Model

To establish the relationship between observed GPS displacements and the signal attributed to load variations, we apply an elastic loading model. Homogeneous half-space models are often used for this goal (Amos et al., 2014; D'Urso & Marmo, 2013); however, Argus et al. (2017) showed that these models overestimate the displacements in the vertical component by a factor of ~2.5. This also affects the horizontal distribution of the uplift signal. Accurately calculating the vertical displacement field is key to the inversion as it can lead to underestimation of the net loading and poor interpretation of the distribution of mass. For this goal, we use the LoadDef software (Martens et al., 2019). LoadDef calculates displacements on a self-gravitating stratified sphere for a given Earth model and allows for complex geometries of the load distributions. This study uses the Preliminary Reference Earth Model (PREM) (Dziewonski & Anderson, 1981). While more detailed Earth models exist [e.g., CRUST 1.0 and CSEM (Fichtner et al., 2018; Laske et al., 2013)], the resulting GPS displacements differ by only fractions of a millimeter between the different Earth models, and estimated loads differ by only a few centimeters. We therefore retain PREM as our Earth model.

3.2 Groundwater Model Setup

Because the effect of the drought does not end at the edge of the lake, our goal is to determine whether additional water loss around GSL contributes to the observed GPS displacements during the drought period. For this purpose, we consider additional rings of loads surrounding the lake. Two constraints are applied to the distribution of loads within individual rings. First, contributions of load variation within bedrock units are assumed to be negligible, so loads are constrained to alluvial units, as identified by the Utah Geologic Unit Map (Hintze et al., 2000). Second, since the basement footwall side of the Wasatch fault to the east sits adjacent to sedimentary layers on the GSL side to the west, it therefore acts as a natural barrier to groundwater. Thus, we prevent loads from crossing the fault to the east. Up to three parallel load rings are tested, each with varying widths between 10 and 45 km. For each unique distribution, Green's functions are calculated with LoadDef for use in the inversion. The randomization of the ring distributions results in 1,889 unique load models tested in this study.

Since we do not expect loads in adjacent rings to differ wildly and because some load rings may contain too many or too few GPS observations, we include a Tikhonov regularization term in our inversion (e.g., Aster et al., 2013). The regularized least squares equation is shown in Equation 1 and our individual load solutions are shown in Equation 2.

$$min\ \|Gm - d\|_2^2 + \alpha\|Lm\|_2^2 \tag{1}$$

$$m_\alpha = (G^T W G + \alpha L^T L)^{-1} G^T W d \tag{2}$$

Here G is our matrix of Green's functions, m contains the loads we are inferring (as equivalent water thickness), d contains our observed GPS displacements, W is the weighting matrix built from the GPS observation uncertainties, L is the roughening matrix for the regularization, and α is the regularization parameter. To find the optimal balance between the regularization and the fit to the data, a range of α values are tested. We choose the best solution from the L-curve for each load distribution, which identifies the regularization parameter which minimizes the solution and residual norms.

3.3 Preferred Groundwater Model

Our primary goal is to minimize the misfit to the displacements, but this does not guarantee the most realistic model, so a few considerations are taken into account to identify the preferred model. First, we omit solutions which exhibit ring loads greater than the inferred load on the lake. The individual loads represent an average load, applied evenly across the surface of each region. Although the average decline in water levels in the wells is higher than the load on the lake, the GSL is likely to exhibit the highest average rate of load variation due to direct evaporation from the surface of GSL itself. Groundwater observations reveal spatial variability in the distribution of loads, indicating non-uniform load variation exterior to the lake. The average load across the surface of each ring is likely to be lower than localized well observations as well as lower than the uniform load change on the lake. Similarly, due to the intensity of the drought and well observations, we do not expect rings to exhibit average net positive loads. Non-positivity is not enforced in the inversion, but solutions with positive loads are simply removed from these results. Of the remaining solutions, we identify those that best minimize the data misfit and also have a GSL load comparable to that observed during the drought.

We find that our preferred model estimates a load of -1.85 ± 0.33 m on the GSL and provides a good fit to both the horizontal and vertical GPS displacements observed, with a 3D RMS misfit of 1.73 mm (Figure 4). This model exhibits two radial load rings. An inner ring of 24 km width with a load of -1.16 ± 0.20 m, and an outer ring of 40 km width with a load of -0.32 ± 0.14 m. The load inferred on the lake itself is very close to the observed -1.89 ± 0.04 m. Inclusion of the groundwater loads provide a more disperse vertical uplift signal and significantly improves the fit to the vertical displacements. This results in a net improvement in the 3D GPS misfit of 30.5%, compared to the model that fixed the observed lake level decline solely to the bounds of the lake. The regularization parameter for our preferred model is 1.75, with the solution sitting well on the corner of the trade-off curve. A comparison of the preferred ring model to the observed and inferred lake only models is shown in Table 1. While the volume inferred on the lake is comparable to that observed (i.e., 5.5 ± 1.0 km^3 versus the observed 5.58 ± 0.11 km^3), the combined volume attributed to groundwater loss surrounding the GSL is twice the lake loss at 10.9 ± 2.8 km^3, spread over an area nearly six times larger than GSL, resulting in a total model volume of -16.5 ± 3.8 km^3. This is nearly five times the volume observed within the spatial resolution of GRACE. The volume we find is consistent across the full set of ring model solutions with a median volume of -15.92 ± 0.71 km^3, at 95% confidence.

4 Regional Seismicity Modulation

We next assess whether the drought-modulated load variations on the Earth's surface is reflected in spatio-temporal variations in seismicity in our study area. We use the Utah Authoritative Region earthquake catalog for 1981 – 2020. Prior to our analysis, the catalog was declustered following Zaliapin & Ben-Zion (2020). Events are limited to only mainshocks that occur to the west of the Wasatch fault. While studies have identified strong correlations between seasonal water level variation and seismicity (Amos et al., 2014; Craig et al., 2017; Kreemer & Zaliapin, 2018), we find no evidence of annual seismicity modulation, in agreement with the findings of Hu & Bürgmann (2020), so we inspect the catalog for evidence of temporally variable, drought-cycle induced seismicity modulation. To allow for an equal assessment of seismicity during wet and dry periods, we cut the catalog to the period of 1987.1 – 2020, in which there are equal timeframes where the PDSI indicates either wet or dry periods. The distribution of earthquakes is shown in Figure 5. Earthquakes are primarily located to the northeast of the lake near the Hansel Valley, Hansel Mountain, and North Promontory faults, and to the south of the lake along the Wasatch fault. Events occurring within the bounds of the lake occur near the ends of the Great Salt Lake fault zone, which runs NW–SE along the eastern edge of the lake and dips to the west.

The trimmed catalog is separated into two sets. The first are those events which occur within the load of the preferred model, shown in light blue. The second reflects the events occurring outside the load region. For an objective comparison of earthquakes occurring inside and outside of the load, the area of the outside region is constrained to be equivalent to that of the load region. Due to the sparsity of events to the west of GSL, the outside region is mostly limited to the area north of the GSL (i.e., up to 42.5°) and south of the GSL. Finally, we set a conservative magnitude cutoff of 1.3, inferred from an inspection of the cumulative and non-cumulative distribution of events within our region. This cutoff magnitude is comparable the findings of Pankow (2004), who found a cutoff magnitude of 1.2 for the GSL basin for the period of 2000 – 2003.

Following these criteria, the cumulative number of events in the study area (i.e., the defined inside and outside areas) between 1987.1 and 2020 is 1,345. We then separate these events depending on whether they occurred during dry and wet periods and whether they are in the area inside or outside the load. This reveals that inside the load area, earthquakes occur ~20% more frequently when the region is experiencing drier conditions, while outside the load area there only being ~2% more events during drier periods (Table 2). While the number of events in this catalog is fairly small, we find that the observed ratio of events during dry over wet periods for the load region is well above the 95%, 1-sided confidence level, following 100,000 temporal randomizations of the catalog. The same ratio outside of the load is not statistically significant. The prevalence of earthquakes during dry time periods identifies modulation of seismicity likely associated with fault unloading due to the reduced mass on the Earth's surface within the load region during dry periods.

To further investigate the temporal aspect of the seismicity near the GSL, we compare the relationship between the surface elevation rate of the lake and the seismicity rate, shown in Figure 6. Each dataset is smoothed with a 3-year moving window to identify long term trends. Regional PDSI is shown in the background, indicating periods of relative dryness and wetness in the study area. Periods which exhibit drier conditions see an increase in seismicity rate as the lake level recedes, and the inverse occurs as the lake fills. Notably, the earthquake rate exhibits periods of distinct trends which are consistent and unique for each individual period. The relationship between the timing of these rate changes is illuminated when compared to the rate of GSL surface elevation change. We see a temporal relationship between changes in the trend of seismicity rate and the inflection of the GSL surface elevation rate. As the surface elevation rate changes sign, a change in the trend of the rate of earthquakes is closely observed. Increasing seismicity trend changes are tied to periods when the lake exhibits negative rates and decreasing seismicity trends relate to periods when the lake is filling. These results further indicate a close relationship between the trends of mass fluctuation within the GSL basin and seismicity.

5 Discussion

We find that the observed drought-induced GPS displacements can best be described by the presence of additional groundwater mass loss surrounding the GSL. When we invert only for the load on GSL itself, we find an unrealistic load on the GSL that is 2.65 times higher than what is observed from the lake level decline. In our preferred model, which includes mass loss outside the GSL, we resolve the observed unloading of GSL between 2012 and 2016. It is possible to produce a model which estimates the load on the lake from the vertical component only, but the 3D inversion produces more consistent estimates. The median GSL load estimate is -1.87 ± 0.15 m compared to -1.75 ± 0.22 m for the vertical only models. Furthermore, the vertical-only inversion produces higher ring estimates. The balance between reduced GSL load estimates and increased ring load estimates, indicates a bias due to the distribution of GPS sites, which is addressed by the inclusion of the horizontal components. We see that the full 3D inversion better localizes the mass to the lake and produces more consistent results.

The estimated volume of water loss is substantial, at 16.4 ± 3.8 km^3, with a ratio of groundwater to surface water volume of 2:1. Differences between the GRACE estimated volume of 3.48 ± 0.21 km^3 and the observed lake volume loss of 5.58 ± 0.11 km^3 can be explained by the spatial resolution of GRACE; however, this leaves significant water level variation observed at nearby wells unaccounted for. Wells within the two inferred load rings reveal a relationship between the ratio of the inferred loads and the observed mean water level change. Table 3 shows the average water level change and range (using three interpretations of the well data during the drought period, see section 2.1) for wells located in each ring. The Theil-Sen approach allows for more well solutions than MIDAS and the results are plotted on Figure 4. All three methods find an average water level change within Ring 1 near -3 m and less water loss in Ring 2. Additionally, the ratio of water loss between the two rings is comparable to the ratio inferred by our model (with 3 – 4 times higher change in water level within the inner ring compared to the outer ring) when the well change is estimated by MIDAS or net difference approaches. While the well observations show that some localized areas exhibit large changes in groundwater levels, they also show a wide range of observed water displacement. Considering that wells are primarily located where water levels are most observable or intriguing, it is likely that water levels in wells reflect above average loss of water compared to the entire surface area of the inferred rings. Furthermore, our inferred rings reflect area averaged loads, which provides insight into the net magnitude of water loss required to explain the GPS displacements, but underestimates the complexity of the real mass distribution. We note that GPS uplift is significantly less to the west of the GSL than east of the GSL (Figure 3), which may reflect greater water loss closer to the Wasatch fault and our inferred load rings provide a more regionally averaged estimate. To better infer the complexity of the real load distribution in future studies, a significantly higher density of long running GPS stations is required than are currently installed such that more complex load distributions can be considered.

Vertical displacements associated with loading signals are largest near the center of the load, while horizontal displacements reach their maximum at the edges of the load (e.g., Becker & Bevis, 2004). Consequently, extension or contraction is expected within the load bounds, depending on the sign of the signal, with the largest change in vertical stresses directly under the load. In the presence of listric normal faults [e.g., the Wasatch fault zone as suggested by Pang et al. (2020) and Savage et al. (1992)], the role of vertical stresses on faults is increased at depth when the fault dip becomes shallower (i.e., less than 45°). Since the majority of events within the catalog do not occur near the surface, we expect higher quantities of events during drier periods, due to the reduction of vertical stresses on the faults cutting underneath the load at depth. This matches well with our findings (Table 2), and we find the strongest distinction between the inside and outside regions with this load distribution. If the actual load were constrained closer to the bounds of the lake, or to a much wider region around GSL, such a distinction between dry and wet events would not be clear at this specific radial distance. The observed seismicity modulation may therefore corroborate the spatial extent of the load implied by our model. While a cutoff magnitude of 1.3 is used in this study, observed seismicity trends are also found when using magnitudes above 0.8, but they are only significant (at the 95% confidence level) when considering events with magnitudes above 1.2 (Figure S3). In fact, the higher the cutoff magnitudes we consider, the higher the difference between dry and wet events within the load region, while the events outside the load continue to reflect no significant trends.

The temporal relationship between seismicity and mass variation is highlighted in Table 4 with correlations between seismicity rates and PDSI, GRACE, and GSL surface elevation rate. A clear distinction exists between inside and outside load events, with those inside exhibiting anti-correlation and those outside showing no relationship. Further comparison of the earthquake rates to lake elevation rates highlights the long-term seismicity modulation in the region (Figure 6). Changes in the trend of earthquake rate in the region alter when the rate of GSL surface elevation changes sign. That is, that as the lake shifts from losing water to gaining water, the seismicity rate changes from negative to positive. These trends are consistent between inversions of the lake elevation rate and are unique for each time period, supporting an inverse relationship between load variation and seismicity.

This study advances the findings of Elósegui et al., 2003, and further distinguishes the contribution the GSL and surrounding groundwater make to regional water loss during droughts. As noted in their study, load geometry plays a significant role in best explaining the GPS observations and the placement of loads determines which signals will be constructive or deconstructive at each site. Significantly higher complexity of load distribution is applied in this study than their two disk model; however, the real distribution of groundwater loads is undoubtedly still more complex. This likely explains some of the residuals exhibited at GPS sites to the south of the GSL where wells exhibit increased spatial variability of water level change and localized aquifers have been shown to alter the deformation field (Hu & Bürgmann, 2020). Nevertheless, the simple distribution of surface averaged groundwater loss in addition to the unloading of the GSL, provides significant improvement to the interpretation of GPS data near the GSL. The results of this study highlight that mass variability on local scales have a significant impact on GPS timeseries and must be accounted for when, for example, using those data to infer secular loading rates on nearby faults.

6 Conclusions

The results presented in this study find that GPS data are able to observe and localize mass loss within the GSL basin and that the regional extent of inferred water loss during the drought period is supported by both regional seismicity variations and well observations. Inclusion of two surface averaged groundwater rings in the inversion, covering a radial distance of 64 km from the lake, significantly improve the fit to the GPS observations. We find the inferred groundwater loss to be substantial (10.9 ± 2.8 km^3), at twice the volume observed on the lake (5.58 ± 0.11 km^3), and are able to recover the lake observation with an inferred lake volume loss of 5.5 ± 1.0 km^3. The modeled ratio of groundwater to surface water estimates is comparable to the findings of Castle et al. (2014) and Ojha et al. (2019) where groundwater loss exceeded surface water loss at a rate 1.89 – 4.79 times higher, during the same drought. Additionally, wells within our inferred load region corroborate the presence of significant water level decline, and the ratio between average well water levels and inferred loads, between the inner and outer rings, are comparable.

We find that earthquakes within the load region occur during dry versus wet periods ~20% more frequently and that the earthquake rate is anti-correlated with the PDSI, GRACE, and lake elevation rate, with coefficients of -0.45, -0.55, and -0.52 respectively. Events outside the load show no significant relationships. These results reveal a long-term relationship between the distribution and variation of loads with stresses on faults, resulting in drought-cycle influenced seismicity modulation within the loaded region.

Our study benefits greatly from the distribution of long running GPS stations near the GSL, which directly improved the performance of the inversion and advances the finding of Elósegui et al., 2003. Future modeling of load variation on and near GSL will be greatly improved by the quantity of GPS stations which have been installed in the past 10 years, although there remains no nearby GPS sites to the west of the lake. Additionally, the expansion of the GPS network will reduce uncertainty in load estimates and allow for more complex load geometries. Our case study for the GSL, highlights how regional GPS networks are particularly well suited to identify water loss in similarly sized lakes and reservoirs during drought periods. Continued expansion of GPS networks will further allow water management authorities to identify and quantify regional variation in water storage and its redistribution.

Acknowledgments

We thank H. Martens for her help with the LoadDef software and I. Zaliapin for declustering the earthquake catalog. We are grateful for UNAVCO for the maintenance of the NOTA GPS stations and making the data freely available. This work was supported by NSF grant EAR1615253 and NASA Earth Surface and Interior grant 80NSSC19K1044 to CK and GB. All figures were produced using Generic Mapping Tools (Wessel et al., 2013).

Data Availability Statement

GPS timeseries are available from the Nevada Geodetic Laboratory at geodesy.unr.edu/gps_timeseries/ (Blewitt et al., 2018). GSL surface elevation data can be found courtesy of the USGS at https://waterdata.usgs.gov/nwis/sw, and groundwater well data from the National Ground-Water Monitoring Network through the data portal at https://cida.usgs.gov/ngwmn/. NLDAS solutions are available through the GES DISC at https://disc.gsfc.nasa.gov/datasets/NLDAS_NOAH0125_M_002/summary. PDSI data from the West Wide Drought Tracker can be downloaded at https://wrcc.dri.edu/wwdt/batchdownload.php. CSR, GFZ, and JPL GRACE RL06 solutions are available through the PODAAC archive (NASA Jet Propulsion Laboratory (JPL), 2019a, 2019b, 2019c). The earthquake catalog can be found through the University of Utah at https://quake.utah.edu/earthquake-information-products/earthquake-catalogs. MIDAS software is available at http://geodesy.unr.edu/ (Blewitt et al., 2016), and the LoadDef software is available at https://github.com/hrmartens/LoadDef (Martens et al., 2019).

475 ## References

Abatzoglou, J. T., McEvoy, D. J., & Redmond, K. T. (2017). The West Wide Drought Tracker: Drought Monitoring at Fine Spatial Scales. *Bulletin of the American Meteorological Society*, *98*(9), 1815–1820. https://doi.org/10.1175/BAMS-D-16-0193.1

Amos, C. B., Audet, P., Hammond, W. C., Bürgmann, R., Johanson, I. A., & Blewitt, G. (2014). Uplift and seismicity driven by groundwater depletion in central California. *Nature*, *509*(7501), 483–486. https://doi.org/10.1038/nature13275

Argus, D. F., Landerer, F. W., Wiese, D. N., Martens, H. R., Fu, Y., Famiglietti, J. S., et al. (2017). Sustained Water Loss in California's Mountain Ranges During Severe Drought From 2012 to 2015 Inferred From GPS. *Journal of Geophysical Research: Solid Earth*, *122*(12), 10,559-10,585. https://doi.org/10.1002/2017JB014424

Aster, R., Borchers, B., & Thurber, C. (2013). Chapter Four - Tikhonov Regularization. In *Parameter Estimation and Inverse Problems* (Second Edition, p. Pages 93-127). Academic Press.

Becker, J. M., & Bevis, M. (2004). Love's problem. *Geophysical Journal International*, *156*(2), 171–178. https://doi.org/10.1111/j.1365-246X.2003.02150.x

Blewitt, G., Kreemer, C., Hammond, W. C., & Gazeaux, J. (2016). MIDAS robust trend estimator for accurate GPS station velocities without step detection. *Journal of Geophysical Research: Solid Earth*, *121*(3), 2054–2068. https://doi.org/10.1002/2015JB012552

Blewitt, G., Hammond, W., & Kreemer, C. (2018). Harnessing the GPS Data Explosion for Interdisciplinary Science. *Eos*, *99*. https://doi.org/10.1029/2018EO104623

Borsa, A. A., Agnew, D. C., & Cayan, D. R. (2014). Ongoing drought-induced uplift in the western United States. *Science*, *345*(6204), 1587–1590. https://doi.org/10.1126/science.1260279

Castle, S. L., Thomas, B. F., Reager, J. T., Rodell, M., Swenson, S. C., & Famiglietti, J. S. (2014). Groundwater depletion during drought threatens future water security of the Colorado River Basin. *Geophysical Research Letters*, *41*(16), 5904–5911. https://doi.org/10.1002/2014GL061055

Craig, T. J., Chanard, K., & Calais, E. (2017). Hydrologically-driven crustal stresses and seismicity in the New Madrid Seismic Zone. *Nature Communications*, *8*(1), 2143. https://doi.org/10.1038/s41467-017-01696-w

D'Urso, M. G., & Marmo, F. (2013). On a generalized Love's problem. *Computers & Geosciences*, *61*, 144–151. https://doi.org/10.1016/j.cageo.2013.09.002

Dziewonski, A. M., & Anderson, D. L. (1981). Preliminary reference Earth model. *Physics of the Earth and Planetary Interiors*, *25*(4), 297–356. https://doi.org/10.1016/0031-9201(81)90046-7

Elósegui, P., Davis, J. L., Mitrovica, J. X., Bennett, R. A., & Wernicke, B. P. (2003). Crustal loading near Great Salt Lake, Utah. *Geophysical Research Letters*, *30*(3). https://doi.org/10.1029/2002GL016579

Famiglietti, J. S. (2014). The global groundwater crisis. *Nature Climate Change*, *4*(11), 945–948. https://doi.org/10.1038/nclimate2425

Famiglietti, J. S., Lo, M., Ho, S. L., Bethune, J., Anderson, K. J., Syed, T. H., et al. (2011). Satellites measure recent rates of groundwater depletion in California's Central Valley. *Geophysical Research Letters*, *38*(3). https://doi.org/10.1029/2010GL046442

Famiglietti, James S., & Rodell, M. (2013). Water in the Balance. *Science*, *340*(6138), 1300–1301. https://doi.org/10.1126/science.1236460

Fichtner, A., van Herwaarden, D.-P., Afanasiev, M., Simutė, S., Krischer, L., Çubuk-Sabuncu, Y., et al. (2018). The Collaborative Seismic Earth Model: Generation 1. *Geophysical Research Letters*, *45*(9), 4007–4016. https://doi.org/10.1029/2018GL077338

Fu, Y., Argus, D. F., Freymueller, J. T., & Heflin, M. B. (2013). Horizontal motion in elastic response to seasonal loading of rain water in the Amazon Basin and monsoon water in Southeast Asia observed by GPS and inferred from GRACE: HORIZONTAL SEASONAL MOTIONS BY GPS/GRACE. *Geophysical Research Letters*, *40*(23), 6048–6053. https://doi.org/10.1002/2013GL058093

Gleeson, T., Wada, Y., Bierkens, M. F. P., & van Beek, L. P. H. (2012). Water balance of global aquifers revealed by groundwater footprint. *Nature*, *488*(7410), 197–200. https://doi.org/10.1038/nature11295

Hassibe, W. R., & Keck, W. G. (1991). *The Great Salt Lake*. U.S Department of the Interior, U.S. Geological Survey. Retrieved from https://books.google.com/books?id=F13LpLqW-EwC

Hintze, L., Willis, G., Laes, D., Sprinkel, D., & Brown, K. (2000). DIGITAL GEOLOGIC MAP OF UTAH Compiled by.

Hu, X., & Bürgmann, R. (2020). Aquifer deformation and active faulting in Salt Lake Valley, Utah, USA. *Earth and Planetary Science Letters*, *547*, 116471. https://doi.org/10.1016/j.epsl.2020.116471

Huber, P. (1981). *Robust statistics*. Wiley, New York.

Kreemer, C., & Blewitt, G. (2021). Robust estimation of spatially varying common-mode components in GPS time-series. *Journal of Geodesy*, *95*(1), 13. https://doi.org/10.1007/s00190-020-01466-5

Kreemer, C., & Zaliapin, I. (2018). Spatiotemporal Correlation Between Seasonal Variations in Seismicity and Horizontal Dilatational Strain in California. *Geophysical Research Letters*, *45*(18), 9559–9568. https://doi.org/10.1029/2018GL079536

Landerer, F. W., & Swenson, S. C. (2012). Accuracy of scaled GRACE terrestrial water storage estimates. *Water Resources Research*, *48*(4). https://doi.org/10.1029/2011WR011453

Laske, G., Masters, G., Ma, Z., & Pasyanos, M. (2013). Update on CRUST1.0 - A 1-degree global model of Earth's crust. *Abstract EGU2013-2658 Presented at 2013 Geophys. Res. Abstracts 15*, *15*, 2658.

Li, W., Jiang, W., Li, Z., Chen, H., Chen, Q., Wang, J., & Zhu, G. (2020). Extracting Common Mode Errors of Regional GNSS Position Time Series in the Presence of Missing Data by Variational Bayesian Principal Component Analysis. *Sensors*, *20*(8), 2298. https://doi.org/10.3390/s20082298

Márquez-Azúa, B., & DeMets, C. (2003). Crustal velocity field of Mexico from continuous GPS measurements, 1993 to June 2001: Implications for the neotectonics of Mexico. *Journal of Geophysical Research: Solid Earth*, *108*(B9). https://doi.org/10.1029/2002JB002241

Martens, H. R., Rivera, L., & Simons, M. (2019). LoadDef: A Python-Based Toolkit to Model Elastic Deformation Caused by Surface Mass Loading on Spherically Symmetric Bodies. *Earth and Space Science*, *6*(2), 311–323. https://doi.org/10.1029/2018EA000462

Mocko, D. (2012). NLDAS Noah Land Surface Model L4 Monthly 0.125 x 0.125 degree, Version 002 [Data set]. NASA Goddard Earth Sciences Data and Information Services Center. https://doi.org/10.5067/NOXZSD0Z6JGD

NASA Jet Propulsion Laboratory (JPL). (2019a). CSR TELLUS GRACE Level-3 Monthly LAND Water-Equivalent-Thickness Surface-Mass Anomaly Release 6.0 in netCDF/ASCII/Geotiff Formats [Data set]. NASA Physical Oceanography DAAC. https://doi.org/10.5067/TELND-3AC06

NASA Jet Propulsion Laboratory (JPL). (2019b). GFZ TELLUS GRACE Level-3 Monthly LAND Water-Equivalent-Thickness Surface-Mass Anomaly Release 6.0 in netCDF/ASCII/Geotiff Formats [Data set]. NASA Physical Oceanography DAAC. https://doi.org/10.5067/TELND-3AG06

NASA Jet Propulsion Laboratory (JPL). (2019c). JPL TELLUS GRACE Level-3 Monthly LAND Water-Equivalent-Thickness Surface-Mass Anomaly Release 6.0 in netCDF/ASCII/Geotiff Formats [Data set]. NASA Physical Oceanography DAAC. https://doi.org/10.5067/TELND-3AJ06

NGWMN. (2020). National Ground-Water Monitoring Network. Retrieved January 19, 2021, from https://cida.usgs.gov/ngwmn/

Ojha, C., Werth, S., & Shirzaei, M. (2019). Groundwater Loss and Aquifer System Compaction in San Joaquin Valley During 2012–2015 Drought. *Journal of Geophysical Research: Solid Earth*, *124*(3), 3127–3143. https://doi.org/10.1029/2018JB016083

Pang, G., Koper, K. D., Mesimeri, M., Pankow, K. L., Baker, B., Farrell, J., et al. (2020). Seismic Analysis of the 2020 Magna, Utah, Earthquake Sequence: Evidence for a Listric Wasatch Fault. *Geophysical Research Letters*, *47*(18), e2020GL089798. https://doi.org/10.1029/2020GL089798

Pankow, K. L. (2004). Triggered Seismicity in Utah from the 3 November 2002 Denali Fault Earthquake. *Bulletin of the Seismological Society of America*, *94*(6B), S332–S347. https://doi.org/10.1785/0120040609

Pekel, J.-F., Cottam, A., Gorelick, N., & Belward, A. S. (2016). High-resolution mapping of global surface water and its long-term changes. *Nature*, *540*(7633), 418–422. https://doi.org/10.1038/nature20584

Rodell, M., & Famiglietti, J. S. (1999). Detectability of variations in continental water storage from satellite observations of the time dependent gravity field. *Water Resources Research*, *35*(9), 2705–2723. https://doi.org/10.1029/1999WR900141

Rodell, M., Famiglietti, J. S., Wiese, D. N., Reager, J. T., Beaudoing, H. K., Landerer, F. W., & Lo, M.-H. (2018). Emerging trends in global freshwater availability. *Nature*, *557*(7707), 651–659. https://doi.org/10.1038/s41586-018-0123-1

Rodell, M., Velicogna, I., & Famiglietti, J. S. (2009). Satellite-based estimates of groundwater depletion in India. *Nature*, *460*(7258), 999–1002. https://doi.org/10.1038/nature08238

Russo, T. A., & Lall, U. (2017). Depletion and response of deep groundwater to climate-induced pumping variability. *Nature Geoscience*, *10*(2), 105–108. https://doi.org/10.1038/ngeo2883

Sakumura, C., Bettadpur, S., & Bruinsma, S. (2014). Ensemble prediction and intercomparison analysis of GRACE time-variable gravity field models. *Geophysical Research Letters*, *41*(5), 1389–1397. https://doi.org/10.1002/2013GL058632

Savage, J. C., Lisowski, M., & Prescott, W. H. (1992). Strain accumulation across the Wasatch Fault near Ogden, Utah. *Journal of Geophysical Research: Solid Earth*, *97*(B2), 2071–2083. https://doi.org/10.1029/91JB02798

Scanlon, B. R., Faunt, C. C., Longuevergne, L., Reedy, R. C., Alley, W. M., McGuire, V. L., & McMahon, P. B. (2012). Groundwater depletion and sustainability of irrigation in the US High Plains and Central Valley. *Proceedings of the National Academy of Sciences*, *109*(24), 9320–9325. https://doi.org/10.1073/pnas.1200311109

Sen, P. K. (1968). Estimates of the Regression Coefficient Based on Kendall's Tau. *Journal of the American Statistical Association*, *63*(324), 1379–1389. https://doi.org/10.1080/01621459.1968.10480934

Serpelloni, E., Faccenna, C., Spada, G., Dong, D., & Williams, S. D. P. (2013). Vertical GPS ground motion rates in the Euro-Mediterranean region: New evidence of velocity gradients at different spatial scales along the Nubia-Eurasia plate boundary. *Journal of Geophysical Research: Solid Earth*, *118*(11), 6003–6024. https://doi.org/10.1002/2013JB010102

Theil, H. (1950). A rank-invariant method of linear and polynomial regression analysis, 1-2; confidence regions for the parameters of linear regression equations in two, three and more variables. *Indagationes Mathematicae*, *1*(2). Retrieved from https://ir.cwi.nl/pub/18446

Tiwari, V. M., Wahr, J., & Swenson, S. (2009). Dwindling groundwater resources in northern India, from satellite gravity observations. *Geophysical Research Letters*, *36*(18). https://doi.org/10.1029/2009GL039401

USGS Water Resources. (2020). USGS Surface-Water Daily Data for the Nation. Retrieved January 25, 2021, from https://waterdata.usgs.gov/nwis/dv/?referred_module=sw

Vörösmarty, C. J., Green, P., Salisbury, J., & Lammers, R. B. (2000). Global Water Resources: Vulnerability from Climate Change and Population Growth. *Science*, *289*(5477), 284–288. https://doi.org/10.1126/science.289.5477.284

Wahr, J., Khan, S. A., Dam, T. van, Liu, L., Angelen, J. H. van, Broeke, M. R. van den, & Meertens, C. M. (2013). The use of GPS horizontals for loading studies, with applications to northern California and southeast Greenland. *Journal of Geophysical Research: Solid Earth*, *118*(4), 1795–1806. https://doi.org/10.1002/jgrb.50104

Wang, J. (2018). Recent global decline in endorheic basin water storages. *Nature Geoscience*, *11*, 10.

Wessel, P., Smith, W. H. F., Scharroo, R., Luis, J., & Wobbe, F. (2013). Generic Mapping Tools: Improved Version Released. *Eos, Transactions American Geophysical Union*, *94*(45), 409–410. https://doi.org/10.1002/2013EO450001

Wurtsbaugh, W. A., Miller, C., Null, S. E., DeRose, R. J., Wilcock, P., Hahnenberger, M., et al. (2017). Decline of the world's saline lakes. *Nature Geoscience*, *10*(11), 816–821. https://doi.org/10.1038/ngeo3052

Xia, Y., Mitchell, K., Ek, M., Sheffield, J., Cosgrove, B., Wood, E., et al. (2012). Continental-scale water and energy flux analysis and validation for the North American Land Data Assimilation System project phase 2 (NLDAS-2): 1. Intercomparison and application of model products. *Journal of Geophysical Research: Atmospheres*, *117*(D3). https://doi.org/10.1029/2011JD016048

Zaliapin, I., & Ben-Zion, Y. (2020). Earthquake Declustering Using the Nearest-Neighbor Approach in Space-Time-Magnitude Domain. *Journal of Geophysical Research: Solid Earth*, *125*(4), e2018JB017120. https://doi.org/10.1029/2018JB017120

Tables

Model	Region	Load (m)	Volume (km^3)	3D RMS (mm)
Observed GSL	GSL	-1.89 ± 0.04	-5.58 ± 0.11	2.49
Solved GSL	GSL	-5.01 ± 0.26	-14.8 ± 0.8	1.85
Preferred Ring Model	GSL	-1.85 ± 0.33	-5.5 ± 1.0	1.73
	Ring 1 – 24 km	-1.16 ± 0.20	-7.5 ± 1.3	
	Ring 2 – 40 km	-0.32 ± 0.14	-3.5 ± 1.5	
		Total Volume	-16.5 ± 3.8	

Table 1: Comparisons between the observed GSL load model (fixed to -1.89 m), the solved GSL load model (inferred at -5.01 m), and the preferred ring model.

Earthquake Counts by Region	Dry Periods	Wet Periods	Expected Median	Observed Ratio	95% Confid. in expected Ratio
Inside Load	444	369	406	1.20	1.15
Outside Load	269	263	266	1.02	1.19
Combined	713	632	672	1.13	1.12

Table 2: Regional earthquakes for the timeframe of 1987.1 – 2020. Dry and wet periods are defined by the PDSI value at the time of the events. Expected median and confidence ratio are calculated from 100,000 randomizations of the catalog. The inside load exhibits significantly more events during dry periods than during wet periods.

Method	Location	Number of Wells	Mean Water Level Change (m)	Median Water Level Change (m)	Water Level Range (m)	
Theil-Sen	Ring 1	9	-3.25	-2.98	-6.21	-0.28
	Ring 2	13	-2.39	-1.77	-9.34	-0.45
MIDAS	Ring 1	4	-3.04	-3.78	-4.37	-0.25
	Ring 2	5	-0.77	-0.11	-3.16	0.32
Net Difference 2012 - 2016	Ring 1	9	-2.98	-2.47	-7.34	-0.24
	Ring 2	13	-1.00	-1.00	-3.87	0.61

Table 3: Comparison of observed groundwater level changes with respect to location within the inferred load rings. Three methods are tested to quantify the observed water deviation during the drought: the Theil-Sen slope estimate, the MIDAS algorithm, and a net difference between the start and end of the drought. For the Theil-Sen and MIDAS solutions, only wells with water level differences greater than two sigma are presented. The net difference solutions take the difference in the average position of 2012 ± 0.1 and 2016 ± 0.1. Each method finds a higher average water loss within the bounds of Ring 1 compared to Ring 2. The ring ratios for both MIDAS and net difference approaches is comparable to the ratio of the ring loads inferred in our model.

	Correlation Coefficient		
Earthquake Rate by Region	PDSI	GRACE	Lake Elevation Rate
Inside Load	-0.45	-0.55	-0.52
Outside Load	-0.01	-0.18	-0.19
Combined	-0.34	-0.51	-0.45

Table 4: Correlation coefficients between PDSI, GRACE, and lake elevation rate with the rate of earthquakes in each region. The distribution of the inside load and outside load regions are shown in Figure 5, and the total represents the combination of these regions.

Figures

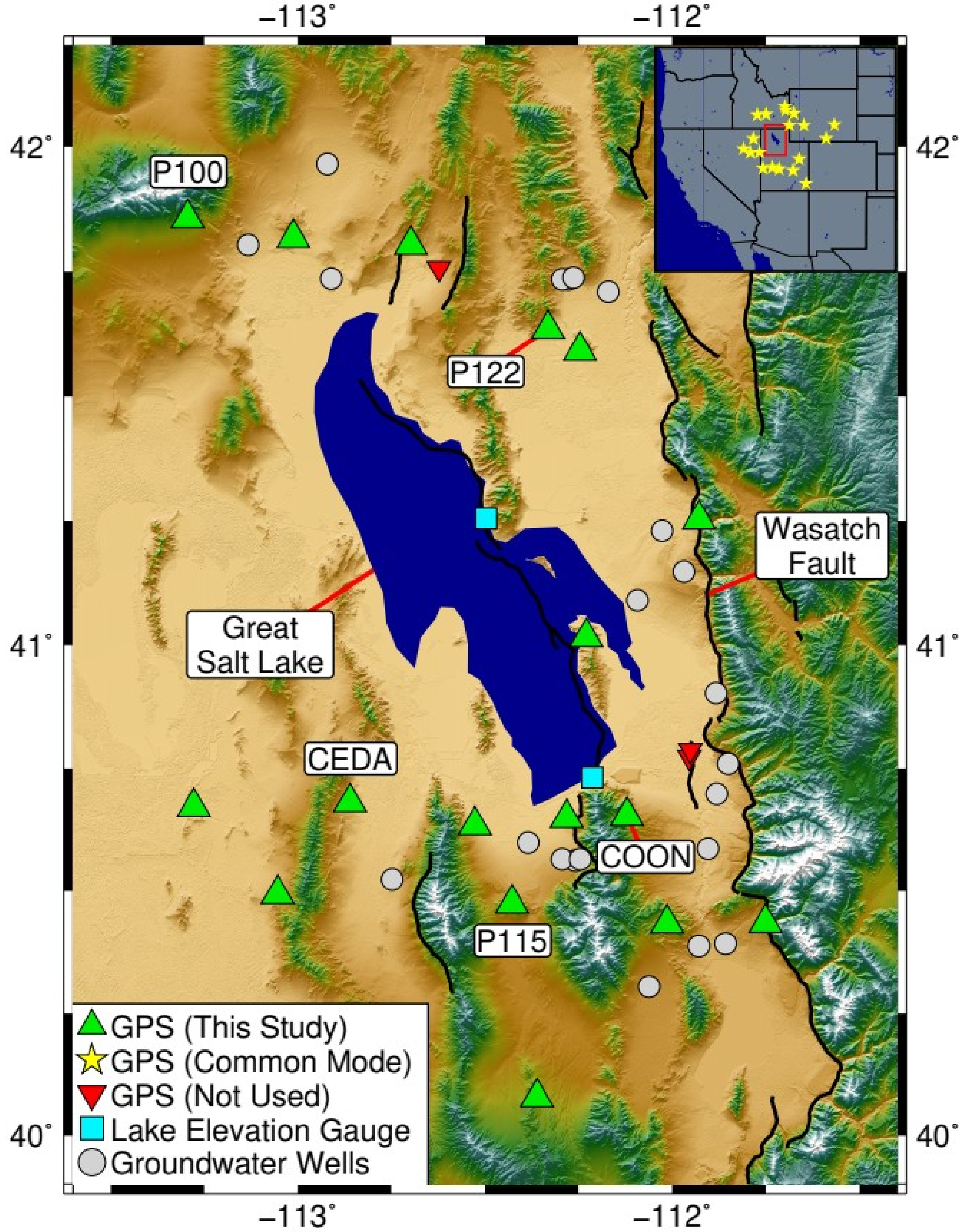

Figure 1: Location map of the study area. Green triangles represent GPS stations included in this study. Red triangles represent GPS stations not included. Turquoise rectangles represent USGS water surface elevation gauges and grey circles represent USGS groundwater well locations. The red box in the inset identifies the bounds of the figure with yellow stars showing the location of stations used to calculate the common mode in the GPS time-series. Labeled stations identify locations of GPS timeseries shown in Figure 2. Black lines represent significant faults in the region, including the Wasatch fault. No data east of the Wasatch fault are included in this study.

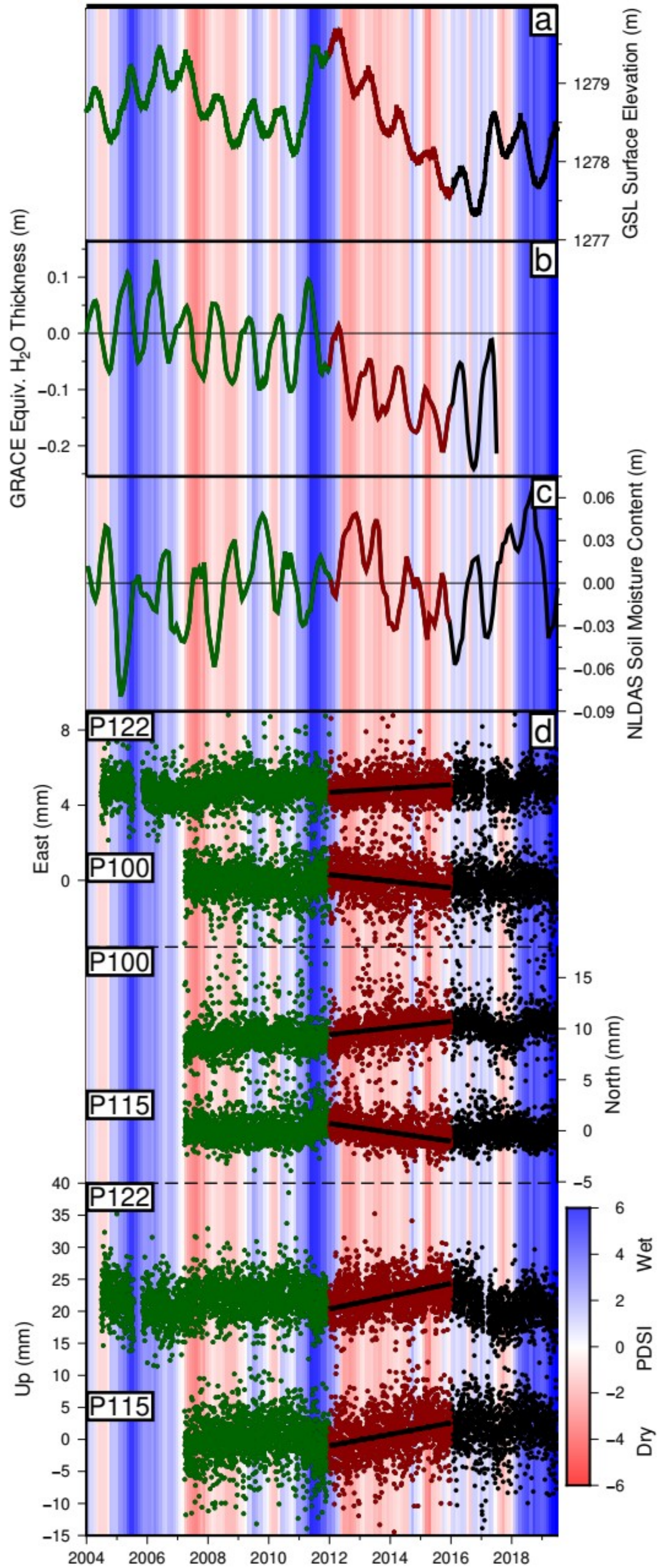

Figure 2: Comparison of GPS, GRACE, PDSI, and GSL surface elevation data. Background shading indicates the Palmer Drought Severity Index averaged over the study area. Green data represent the base period of 2004 – 2012, red data represent the drought period of 2012 – 2016, and black data represents later data not included in this study. **a)** Averaged GRACE data covering a range of 300 km centered on GSL, detrended relative to the base period. **b)** Average of the two GSL water surface elevation stations. **c)** Average NLDAS soil moisture content within the study area. **d)** GPS timeseries detrended relative to the base period. Regional common mode and annual/semi-annual signals have been removed. Station pairs in each component are located on opposite sides of the lake. Black lines represent the trends during the drought period calculated with MIDAS. Stations P122 and P100 show East – West extension, while stations P100 and P115 show North – South extension during the test period. Stations P122 and P115 both show vertical uplift. Station locations are shown in Figure 1.

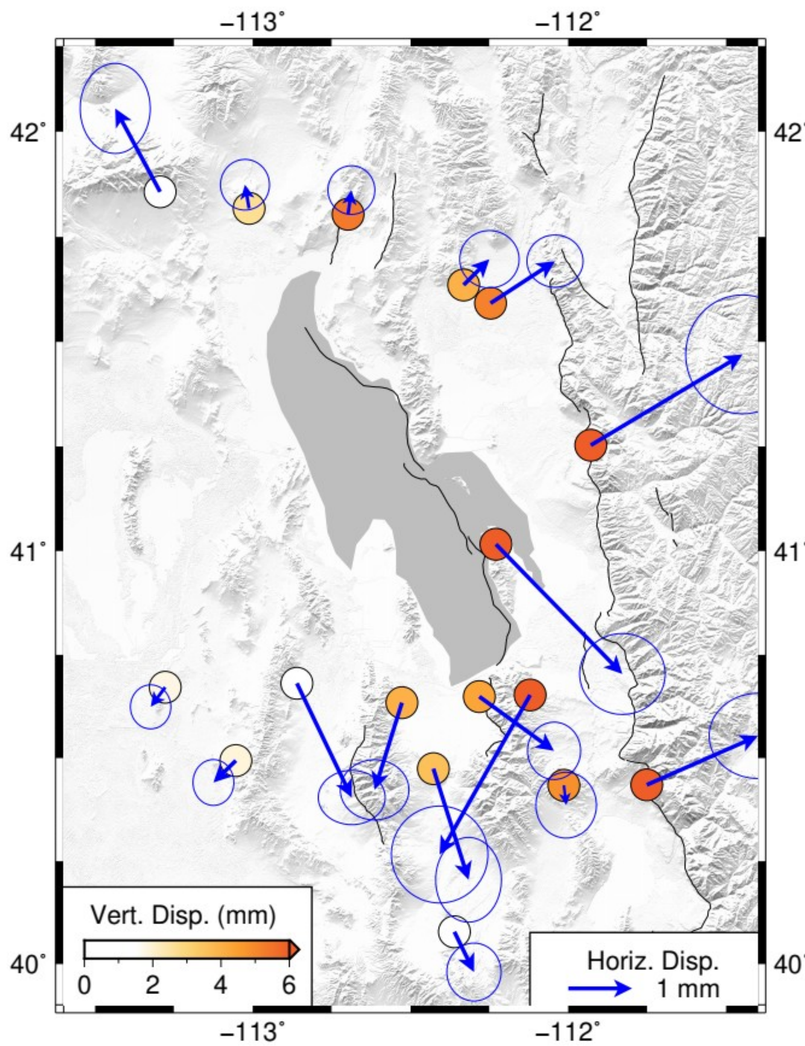

Figure 3: Observed GPS displacements for the drought period (2012 – 2016) relative to the base period (2004 – 2012). Blue arrows represent horizontal displacements with 95% confidence ellipses. Circles represent vertical displacements. Note that horizontal displacements exhibit extension centered on/near GSL, while the largest vertical displacements are located at stations nearest the lake.

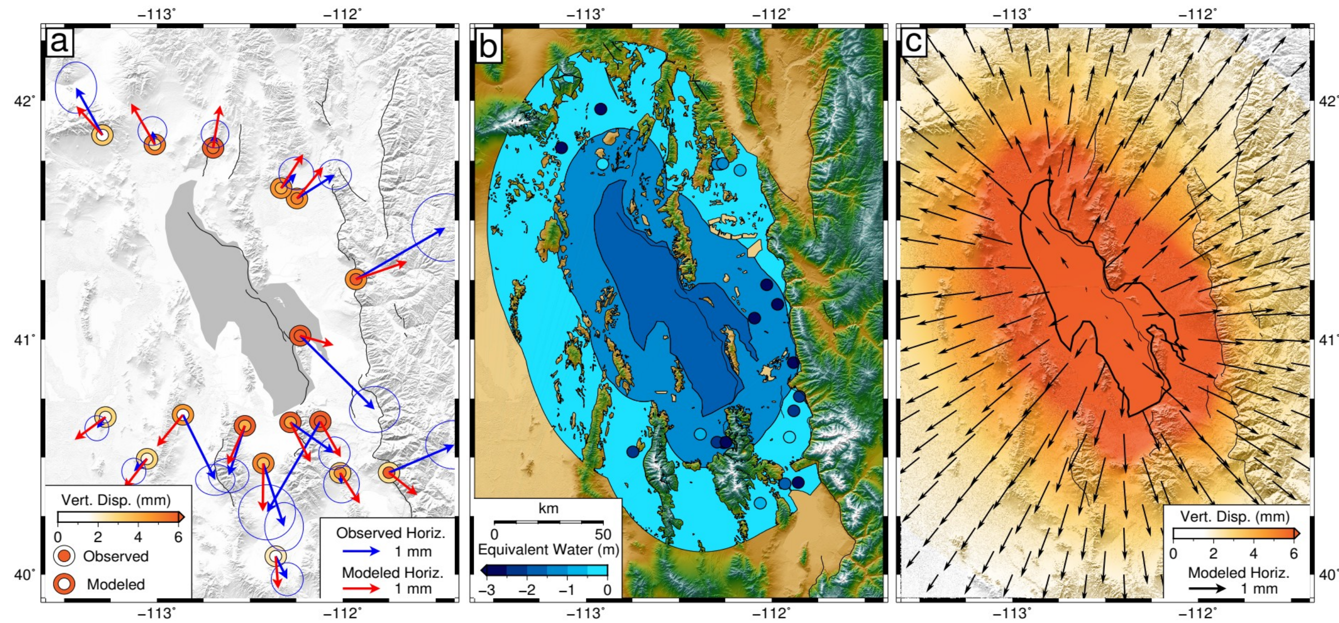

Figure 4: Displacements and distribution of the preferred load model. This model includes the load on GSL and two rings of groundwater at widths of 24 km (inner ring) and 40 km (outer ring). **a)** Comparison of observed and modeled displacements at GPS stations. Blue arrows represent observed horizontal displacements with 95% confidence ellipses. Red arrows represent modeled horizontal displacements. Inner circles represent the observed GPS displacements, while outer circles represent modeled displacements. Faults are represented as thin black lines. The data misfit for this model is 1.73 mm. **b)** Inferred load distribution. Polygon shading represents the load inferred for GSL and two additional rings. GSL load is inferred at -1.85 ± 0.33 m, the inner ring at -1.16 ± 0.20 m, and the outer ring at -0.32 ± 0.14 m. Circles represent changes in groundwater levels observed at wells, with the same color scale as the ring loads. **c)** Modeled displacement field on a grid. Black arrows show horizontal displacements while the background shading shows vertical displacements. The bounds of GSL are shown as the thick black line.

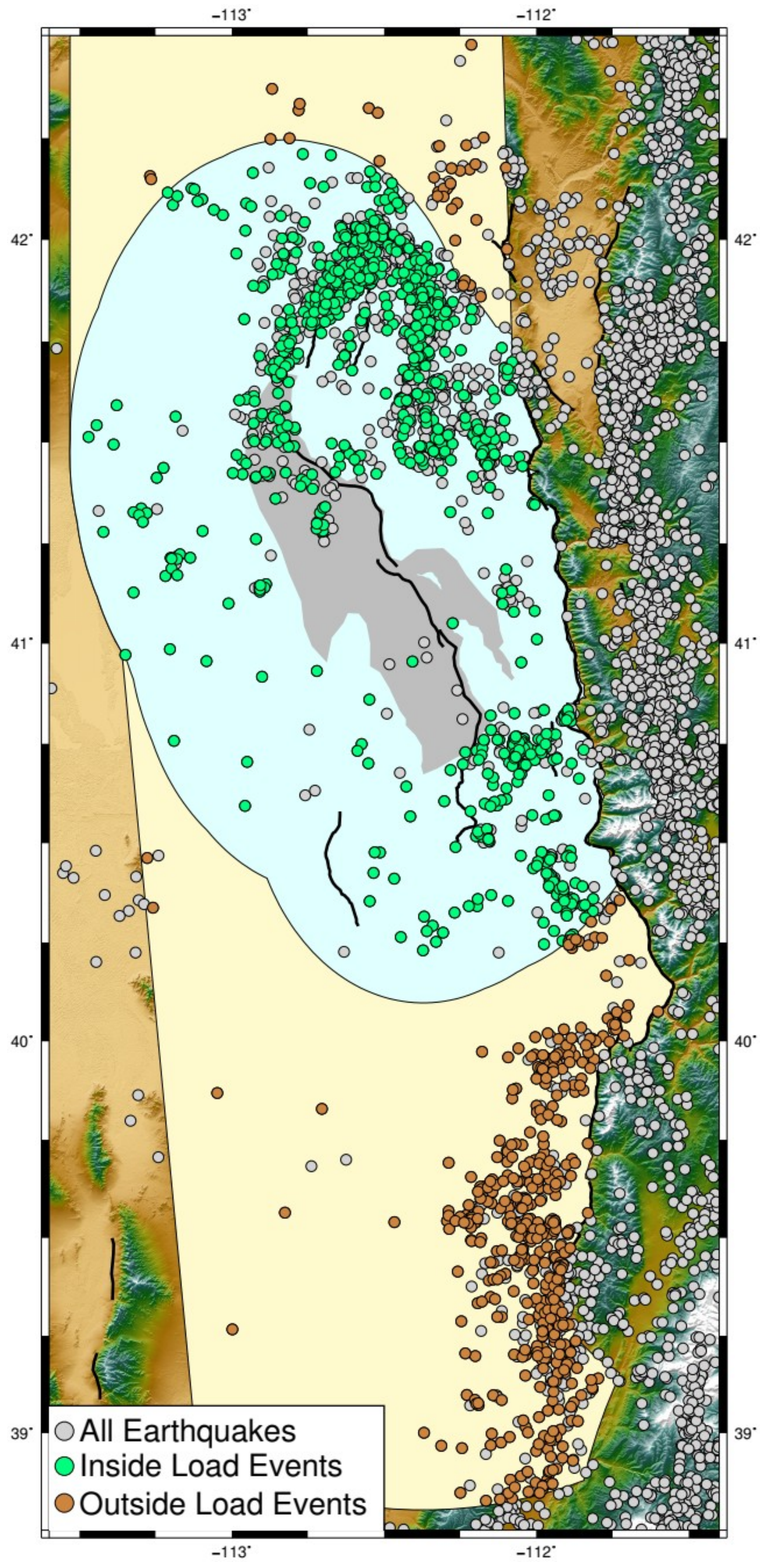

Figure 5: Distribution of regional earthquakes for 1987.1 – 2020. Light blue polygon shows the preferred model load distribution. Light yellow polygon defines the region used to identify earthquakes outside of the load region. The area of this region is equivalent to the area of the modeled load and the northern section ends at 42.5° N. All regional earthquakes are shown as grey circles, those inside of the load and greater than M_W 1.3 are shown as green circles, and those chosen outside of the load and greater than M_W 1.3 are shown as brown circles.

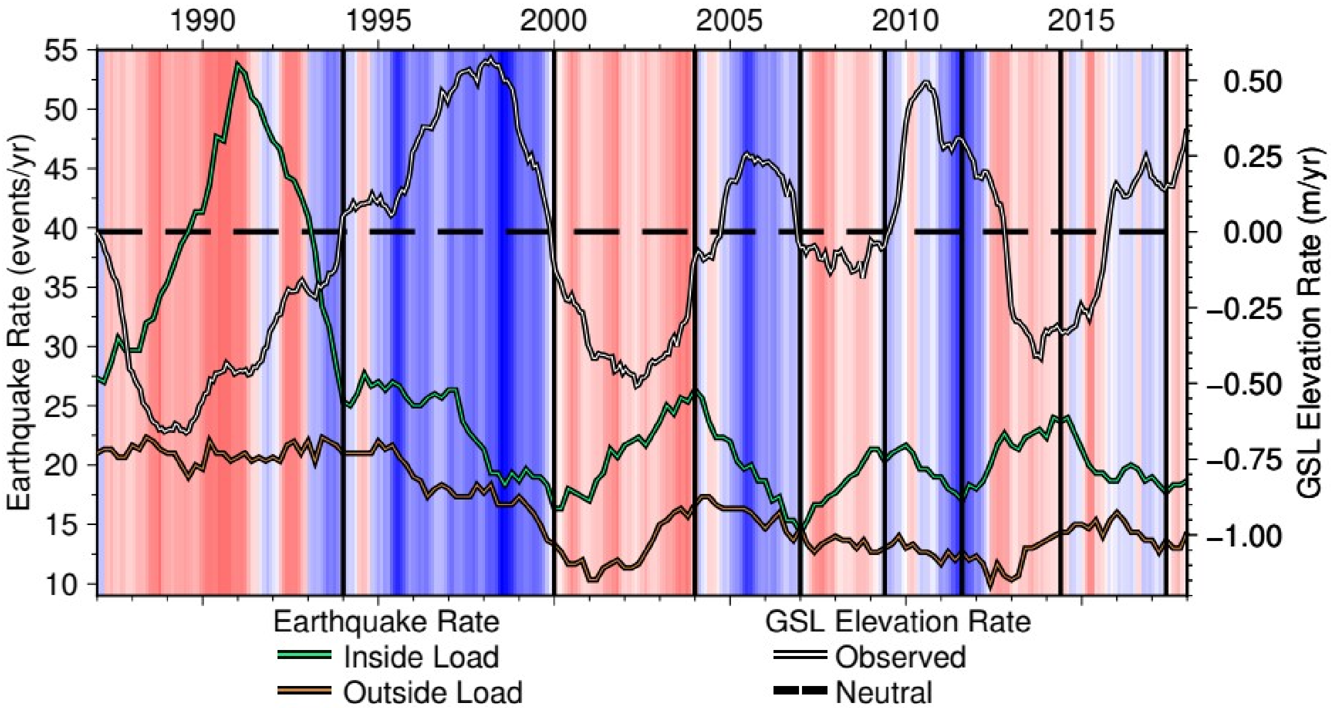

Figure 6: Comparison of earthquake rates for the inside (green) and outside (brown) load regions with the rate of lake elevation change over time (white). Each dataset has been smoothed with a 3-year moving window. Background shading shows PDSI values, scale as shown in Figure 2. Black dashed line represents the neutral line of the GSL elevation rate. Vertical black lines indicate breakpoints for periods of unique trends in the earthquake rate in the inside load area. Note that the timing of the GSL elevation rate inflection often closely matches the timing of changes in the trends of the earthquake rate for the inside load region. Those periods which do not match the inflection better match switches in the PDSI. The outside load region shows minimal variation with the exception of the 1999 – 2004 period.

Journal of Geophysical Research: Solid Earth

Supporting Information for

Drought Induced Groundwater Loss Around Great Salt Lake, Utah, Inferred from 3D GPS Displacements

Zachary Young[1], Corné Kreemer[1], Geoffrey Blewitt[1]

[1]Nevada Geodetic Laboratory, Nevada Bureau of Mines and Geology, University of Nevada, Reno, Reno, Nevada, USA

This supporting information consists of
Figures S1 to S3 and Tables S1 to S4

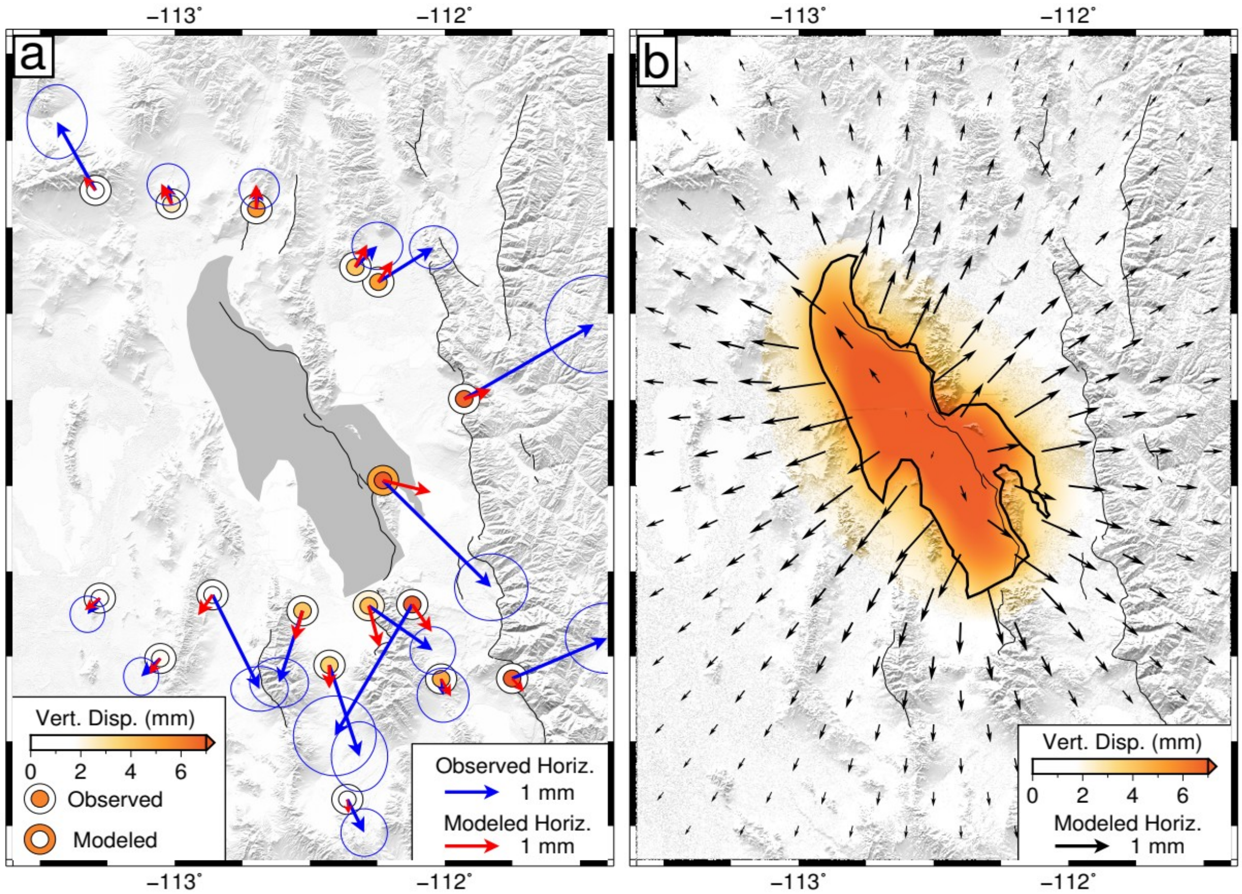

Figure S1.

Modeled displacements for a load equivalent to the observed lake level change between 2012 and 2016 (-1.89 m). Displacements are calculated with LoadDef. Applied load is constrained to the bounds of GSL. **a)** Comparison of observed and modeled displacements at GPS stations. Blue arrows represent observed horizontal displacements with 95% confidence ellipses. Red arrows represent modeled horizontal displacements. Inner circles represent the observed GPS displacements while outer circles represent modeled displacements. Faults are represented as thin black lines. The 3D data misfit for this model is 2.49 mm. **b)** Modeled displacement field on a grid. Black arrows show horizontal displacements, while the background shading shows vertical displacements. The bounds of the region where the load is applied is shown by the thick black line. Note the poor fit to the vertical component.

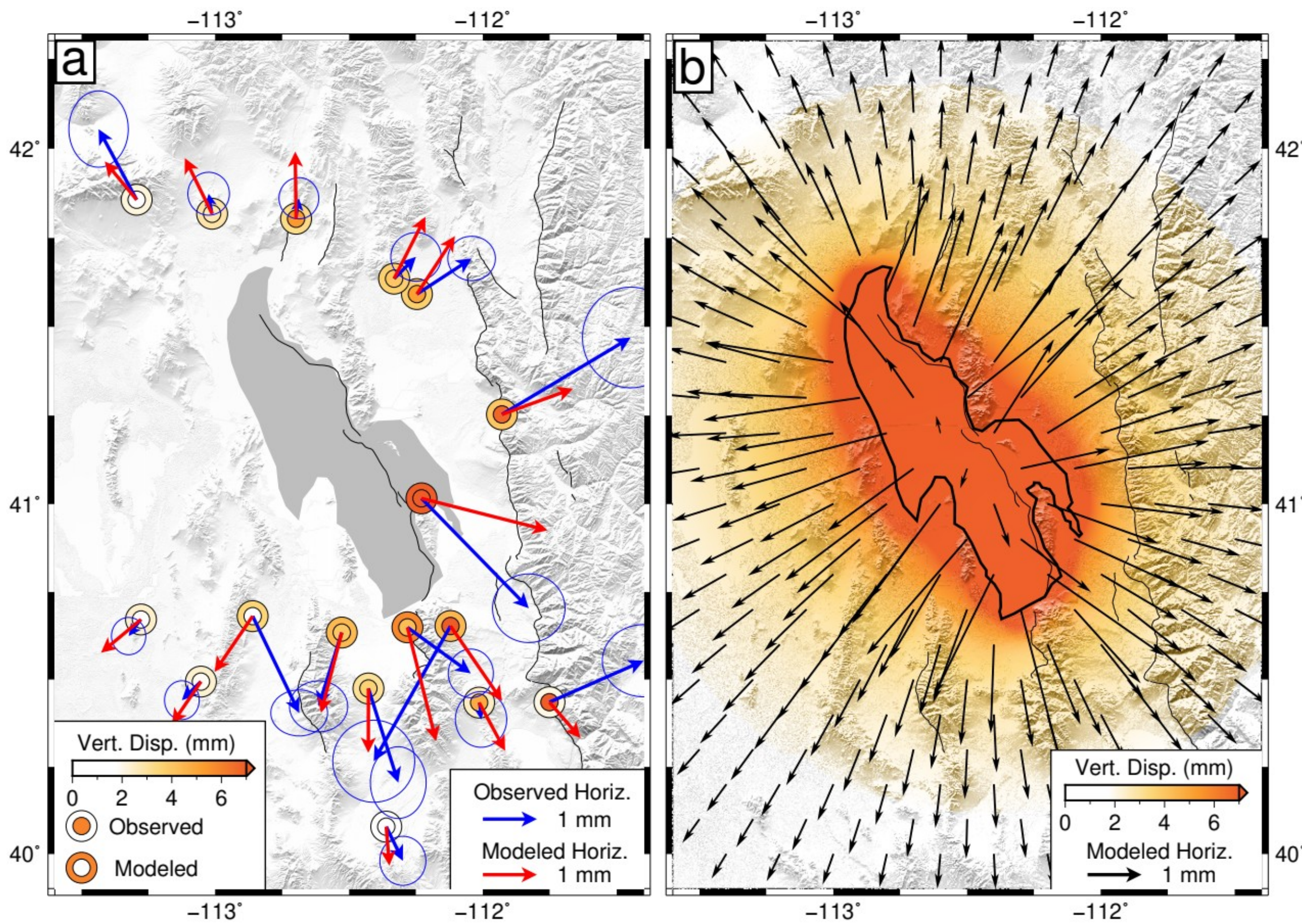

Figure S2.

Modeled displacements for the inferred load on GSL. The distribution of load is constrained to the bounds of GSL and applied equally. Key as described in Figure S1. The inferred load is 5.01 ± 0.26 m with a data misfit of 1.85 mm. Note that the fit improves but the load is significantly higher than the observed GSL water loss and unrealistic.

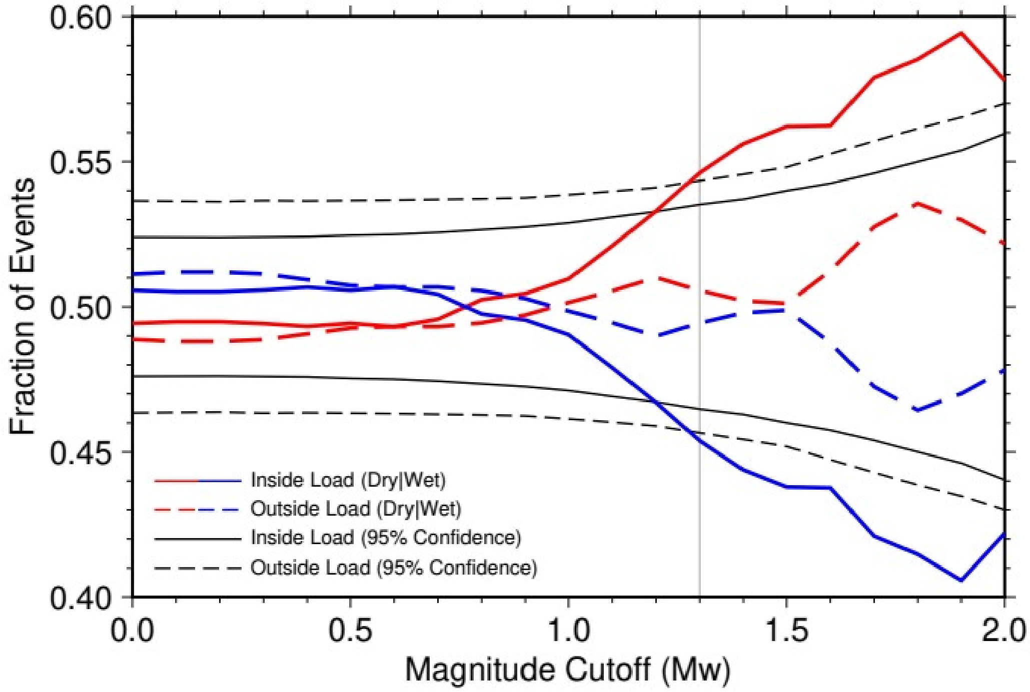

Figure S3.

Confidence level plot comparing dry and wet period events, for the inside and outside load regions, across a range of cutoff magnitudes of the earthquake catalog. Reds indicate events which occur during dry periods as identified by the PDSI. Blues indicate events which occur during wet periods. Solid colored lines reflect events within the inside load region. Dashed colored lines reflect events within the outside load region. Black lines show two sigma confidence bounds for the inside region (solid) and outside region (dashed) following 100,000 randomizations of the catalog at each magnitude. Grey vertical bar reflects the chosen cutoff magnitude of 1.3. Note that for the inside load region, the number of dry events is above the significance level for all magnitudes above 1.2.

				Drought Displacement Calculation Method				
				Theil-Sen		MIDAS		Net Diff.
Well ID	Location	Longitude	Latitude	Water Level Disp. (m)	σ (m)	Water Level Disp. (m)	σ (m)	Water Level Disp. (m)
403339112152501	Ring 1	-112.2588	40.5619	**-3.79**	**0.452**	-4.37	1.06	-3.27
403355112173601	Ring 1	-112.2947	40.5647	**-2.14**	**0.112**	~	~	~
403400112144001	Ring 1	-112.2461	40.5647	**-4.95**	**0.613**	-4.25	0.323	-7.34
403555112230303	Ring 1	-112.3850	40.5986	**-0.84**	**0.102**	~	~	~
403949112043301	Ring 1	-112.0766	40.6636	0.28	0.294	~	~	-0.61
405412111525701	Ring 1	-111.8833	40.9019	**-6.21**	**0.707**	~	~	-6.40
410523112053301	Ring 1	-112.0933	41.0897	**-2.91**	**0.404**	~	~	-2.47
410852111580501	Ring 1	-111.9688	41.1477	**-5.16**	**0.699**	~	~	-3.46
411035111594501	Ring 1	-111.9966	41.1763	-0.22	1.147	~	~	-0.77
411348112013601	Ring 1	-112.0274	41.2299	**-2.98**	**0.931**	-3.30	0.130	-2.24
414411112543701	Ring 1	-112.9111	41.7363	**-0.29**	**0.094**	-0.26	0.002	-0.24
401818112014501	Ring 2	-112.0299	40.3049	0.01	0.065	0.02	0.004	0.02
401818112034201	Ring 2	-112.0624	40.3049	**-0.51**	**0.174**	~	~	~
402317111554401	Ring 2	-111.9292	40.3881	**-1.54**	**0.135**	~	~	~
402333111513401	Ring 2	-111.8579	40.3930	**-3.27**	**1.546**	-3.16	0.075	-3.87
403126112444501	Ring 2	-112.7480	40.5236	**-2.14**	**0.233**	~	~	~
403511111541501	Ring 2	-111.9049	40.5863	**-0.45**	**0.127**	~	~	0.14
403916111575901	Ring 2	-111.9672	40.6544	0.08	0.162	0.32	0.021	0.13
404152111525101	Ring 2	-111.8816	40.6977	**-2.18**	**0.220**	~	~	-1.25
404531111510101	Ring 2	-111.8510	40.7586	**-2.01**	**0.248**	~	~	-1.59
405735112593001	Ring 2	-112.9925	40.9597	-0.06	0.046	~	~	~
411928111581001	Ring 2	-111.9702	41.3244	-0.80	0.548	~	~	0.61
414236112101201	Ring 2	-112.1708	41.7099	**-0.90**	**0.202**	-0.93	0.018	-0.85
414406112163601	Ring 2	-112.2775	41.7349	**-1.77**	**0.060**	~	~	-1.55
414406112173601	Ring 2	-112.2941	41.7349	**-1.16**	**0.159**	~	~	-1.29
414418112154801	Ring 2	-112.2641	41.7383	**-1.27**	**0.269**	~	~	-1.00
414813113075401	Ring 2	-113.1325	41.8035	**-4.55**	**1.072**	~	~	~
415703112514501	Ring 2	-112.8633	41.9508	-0.39	2.343	-0.11	0.022	-0.17
415754112551301	Ring 2	-112.9211	41.9649	**-9.34**	**4.196**	~	~	-2.36

Table S1.

Observed groundwater level change for wells within the inferred load rings by three methods. Water level trends are calculated with Theil-Sen slope estimation method and the MIDAS algorithm and applied to the duration of the drought. The net difference results indicate the difference in the average well water level positions at the start (2012 ± 0.1 yr) and end (2016 ± 0.1 yr) of the drought. Bold Theil-Sen data reflect accepted wells which exhibit water level changes greater than two sigma. All MIDAS values are greater than two sigma.

Station	Longitude	Latitude
AHID	-111.0637	42.2731
BBID	-111.5261	43.6850
BLW2	-109.5578	42.2671
CASP	-106.3841	42.3192
CAST	-110.6773	38.6910
ELKO	-115.8172	40.4147
FOOT	-113.8054	38.8694
GOSH	-114.1797	40.1402
HLID	-114.4140	43.0626
MYT5	-110.0482	39.6027
P007	-114.8197	41.2242
P012	-109.3338	37.5974
P032	-107.2559	41.2417
P684	-111.4505	43.4191
RUBY	-115.1228	40.1172
SMEL	-112.8449	38.9256
SPIC	-112.1275	38.8062
TCSG	-113.4782	43.1192
TSWY	-110.5975	43.1741

Table S2.

GPS stations included in the regional common mode calculation.

			Drought Disp. (mm)			Uncertainty (mm)		
Station	Longitude	Latitude	E	N	U	σ_E	σ_N	σ_U
CEDA	-112.8605	40.6807	0.86	-1.79	0.47	0.21	0.17	0.64
COON	-112.1210	40.6526	-1.42	-2.50	10.34	0.31	0.31	1.25
EOUT	-111.9289	41.2532	2.38	1.42	6.78	0.36	0.38	1.28
LTUT	-112.2468	41.5921	1.01	0.66	5.17	0.18	0.17	0.78
NAIU	-112.2296	41.0157	1.98	-2.04	9.67	0.27	0.26	1.18
P016	-112.3614	40.0781	0.31	-0.63	0.30	0.17	0.19	0.67
P057	-112.6231	41.7566	1.15	0.03	4.88	0.16	0.19	0.68
P084	-113.0540	40.4940	-0.35	-0.34	1.90	0.13	0.15	0.61
P086	-112.2821	40.6488	1.17	-0.85	4.30	0.17	0.18	0.79
P100	-113.2942	41.8568	-0.70	1.31	0.47	0.22	0.29	0.96
P111	-113.0122	41.8173	-0.06	0.37	2.69	0.16	0.16	0.73
P113	-113.2780	40.6713	-0.23	-0.31	1.80	0.13	0.14	0.57
P114	-112.5276	40.6340	-0.43	-1.37	4.00	0.22	0.19	0.78
P115	-112.4280	40.4744	0.55	-1.74	3.59	0.21	0.27	0.89
P116	-112.0142	40.4340	0.04	-0.31	4.84	0.19	0.21	0.73
P117	-111.7514	40.4352	1.74	0.77	10.12	0.31	0.27	1.09
P121	-112.6983	41.8034	0.05	0.38	5.36	0.15	0.16	0.60
P122	-112.3319	41.6354	0.40	0.40	3.99	0.19	0.18	0.79
SLCU	-111.9550	40.7722	4.77	0.93	3.84	0.49	0.33	1.47
ZLC1	-111.9522	40.7860	8.33	-0.78	11.79	0.38	0.25	1.02

Table S3.

Observed GPS relative displacements during the drought period. Values are calculated from the difference of the MIDAS velocities for the drought and base periods then applied to the duration of the drought (four years).

Modeled Displacements at GPS Stations

Station	Longitude	Latitude	Preferred Ring			Observed GSL Only (-1.89 m)			Solve For GSL Only (-5.01m)		
			E	N	U	E	N	U	E	N	U
CEDA	-112.8605	40.6807	-0.69	-0.87	4.66	-0.27	-0.39	1.33	-0.70	-1.03	3.52
COON	-112.1210	40.6526	0.55	-0.99	6.24	0.36	-0.52	1.68	0.95	-1.39	4.44
EOUT	-111.9289	41.2532	1.36	0.48	4.84	0.50	0.18	1.51	1.31	0.48	4.01
LTUT	-112.2468	41.5921	0.68	0.87	4.73	0.27	0.40	1.40	0.70	1.07	3.71
NAIU	-112.2296	41.0157	0.89	-0.27	8.82	0.88	-0.22	5.01	2.34	-0.59	13.29
P016	-112.3614	40.0781	0.07	-0.90	2.32	0.02	-0.27	0.63	0.06	-0.72	1.67
P084	-113.0540	40.4940	-0.62	-0.83	3.00	-0.20	-0.30	0.89	-0.54	-0.79	2.36
P086	-112.2821	40.6488	0.54	-1.11	7.25	0.20	-0.79	2.20	0.53	-2.11	5.84
P100	-113.2942	41.8568	-0.70	0.79	3.36	-0.22	0.27	0.83	-0.59	0.71	2.21
P111	-113.0122	41.8173	-0.64	1.13	5.26	-0.19	0.39	1.09	-0.50	1.03	2.88
P113	-113.2780	40.6713	-0.82	-0.63	2.94	-0.28	-0.23	0.91	-0.74	-0.62	2.41
P114	-112.5276	40.6340	-0.46	-1.08	6.75	-0.15	-0.56	1.67	-0.39	-1.49	4.42
P115	-112.4280	40.4744	-0.02	-1.33	5.11	0.00	-0.45	1.16	0.00	-1.19	3.09
P116	-112.0142	40.4340	0.53	-0.85	3.45	0.18	-0.34	0.94	0.48	-0.89	2.49
P117	-111.7514	40.4352	0.75	-0.62	2.79	0.22	-0.25	0.79	0.57	-0.67	2.09
P121	-112.6983	41.8034	0.18	1.17	6.10	-0.01	0.47	1.24	-0.02	1.24	3.29
P122	-112.3319	41.6354	0.58	0.94	4.80	0.22	0.43	1.40	0.58	1.14	3.71

Table S4.

Displacements at GPS sites, calculated with LoadDef, for the preferred ring load model, the observed fixed GSL load model, and the solved (inferred) GSL load model. The fixed load model only applies the observed load of -1.89 m to the bounds of the lake while the solved GSL model applies the inferred load of -5.01 m. The preferred ring model has a GSL load of -1.85 m, a 24 km inner ring at -1.16 m, and a 40 km outer ring at -0.32 m.